A Tunable Unidirectional Source for GUSTO's Local Oscillator at 4.74 THz

Ali Khalatpour , Andrew K. Paulsen, Sadhvikas J. Addamane, Chris Deimert , John L. Reno, Zbig R. Wasilewski , and Qing Hu

Abstract—The Galactic/Extra Ultra-Long-Duration Balloon Spectroscopic-Stratospheric Terahertz Observatory (GUSTO) is a NASA balloon-borne project and is scheduled for launch in late 2022. The balloon will carry a spectroscopic telescope that will detect three brightest emission lines from the interstellar medium. GUSTO measurements will shed light on the life cycle of the gases in the Milky Way and Large Magellanic Cloud. In this article, we will discuss the details of a quantum cascade laser used in the local oscillator for detecting the oxygen line at 4.74 THz.

Index Terms—THz QCL, GUSTO, Unidirectional DFB, Oxygen line.

I. INTRODUCTION

TERAHERTZ (THz) radiation is loosely defined by the frequency range of 0.5–10 THz (1 THz = 10^{12} cycles/s). The THz spectral range has found unique applications in astronomy owing to a vast amount of THz radiation from the interstellar medium (ISM), the matter between stars consisting of low-density gases and dust in planetary atmospheres [1]. The nitrogen line [NII] at $\approx$ 1.4 THz, the carbon line [CII] at $\approx$ 1.9 THz, and the oxygen line [OI] at $\approx$ 4.7 THz are among the brightest emission lines in the ISM. The [OI] line is rich with information about star formation as it mostly probes warm natural gas heated by massive newborn stars [1]. This spectral line has been inaccessible until recently due to the lack of local oscillators (LOs) in THz frequencies. Take, for instance, far-infrared gas lasers, which only have discrete lines with the closest line 8 GHz away from the 4.744-THz [OI] line [2]. The invention of THz quantum cascade laser (QCL) [3] made it possible to perform heterodyne observation on this line and even map it within the Milky Way galaxy. This line was first detected in the Martian atmosphere using a THz QCL as the LO in 2014 with the high-frequency channel of the far-infrared heterodyne spectrometer *German Receiver for Astronomy at Terahertz Frequencies* on board Stratospheric Observatory for Infrared Astronomy (SOFIA) [4]. Following SOFIA, Stratospheric Terahertz Observatory (STO-2) [5], a NASA balloon-borne mission, was launched from Antarctica in 2016. Once high above the Antarctic (36 km), STO-2 circled along with the polar vortex for a period of three weeks. During that time, STO-2 picked up emission lines at 1.4 and 1.9 THz from (NII) and (CII) lines, respectively. The LO at 4.7 THz based on a THz QCL failed in STO-2 due to an unforeseen technical issue, and no data were collected on the [OI] line. Following up on the STO-2 successful flight, which demonstrated the feasibility of a balloon-borne THz telescope, the Galactic/Extra Ultra-Long-Duration Balloon Spectroscopic-Stratospheric Terahertz Observatory (GUSTO) will be launched in late 2022 [6], [7]. The GUSTO consists of a semiautonomous 0.9-m Cassegrain telescope and cryogenic THz superconducting heterodyne receivers arrays to stay aloft for $\approx$ 100 days. During this time, the GUSTO will survey 124 square degrees of the Milky Way and all of the Large Magellanic Cloud (LMC) in three important interstellar lines with higher angular and velocity resolution compared to previous measurements. The GUSTO is aiming to provide more details on the life cycle of interstellar gas in the Milky Way, formation and destruction of star-forming clouds, the dynamics and gas flow to and in the galactic center, interplay between star formation, stellar winds, and radiation, and the structure of the ISM in the LMC. The GUSTO is a collaborative effort with the Massachusetts Institute of Technology (MIT), University of Arizona, SRON Netherlands Institute for Space Research, Virginia Diodes, Inc., Ball Aerospace, and the Johns Hopkins University Applied Physics Laboratory. In this article, the development of a unidirectional antenna-coupled third-order distributed feedback

Ali Khalatpour, Andrew K. Paulsen, and Qing Hu are with the Department of Electrical Engineering and Computer Science and the Research Laboratory of Electronics, Massachusetts Institute of Technology, Cambridge, MA 02139 USA (e-mail: a.khalatpour@gmail.com; paulsena@mit.edu; qhu@mit.edu).

Sadhvikas J. Addamane and John L. Reno are with the Center of Integrated Nanotechnologies, Sandia National Laboratories, Albuquerque, NM 87185 USA (e-mail: saddama@sandia.gov; jlreno@sandia.gov).

Chris Deimert and Zbig R. Wasilewski are with the Department of Electrical and Computer Engineering, University of Waterloo, Waterloo, ON N2L 3G1, Canada (e-mail: chris.deimert@uwaterloo.ca; zbig.wasilewski@uwaterloo.ca).

TABLE I
GUSTO MINIMUM REQUIREMENTS FOR THE LO AT 4.7 THZ

performance metric	requirements
nominal frequencies (GHz)	4740.0, 4741.6, 4743.6, and 4749.2
c.w. output power	$\geq$1.6 mW at 55 K in single lobe
tunability	$\pm$1.5 GHz at nominal frequencies
heat dissipation	$\leq$2.7 W at 55 K, $\leq$3.5W at 60 K

For the GUSTO, the QCL is cooled with a Sunpower CT cryocooler.

(UADFB) grating [8] for the GUSTO's LO at 4.74 THz is discussed.

II. METHODS AND DISCUSSIONS

A. Required Performance Metrics for the LO at 4.74 THz

In space and suborbital missions, heterodyne receiver arrays allow scientists to map a larger area within limited space mission lifetime. For example, velocity-resolved large-scale images in the fine-structure line of ionized carbon [CII] at 1.9 THz were observed by a 14-pixel heterodyne array receiver on the SOFIA [9]–[11]. In heterodyne receiver arrays, multiple LO beams can be generated from a single beam using a phase grating [12]. The [OI] array for the GUSTO includes 2×4 superconducting hot-electron bolometer (HEB) receivers. The required performance metrics for the LO at 4.7 THz were calculated by researchers at SRON and the University of Arizona to ensure the proper performance of HEB receiver array and phase grating integrated with the optical setup and explained in detail in [13]–[15]. By taking into account the optical loss due to the non-Gaussian beam pattern of THz QCLs, phase grating, and the available cooling power, the overall performance metrics were calculated and are listed in Table I. The continuous frequency tunability is essential for detection of large Doppler shift for mapping in the Milky Way. The lower cooling power in the GUSTO (3.5 W at 60 K) as compared to SOFIA (4 W at 35 K) is mainly due to the limits on weight and heat exchange with environment for sterling coolers in balloon-borne projects (GUSTO) as compared to air-borne projects (SOFIA). This higher operating temperature with lower cooling power posts additional challenges in the LO development. THz QCLs can relatively easily produce $\approx$ 1 mW of continuous wave (c.w.) power at $T \leq 40$ K, but the power drops below 20% for $T \geq 60$ K [10], [11].

B. Photonic Wire Lasers: An Optimized Platform for the GUSTO

As listed in Table I, the 4.7-THz LO for the GUSTO requires long-duration single-mode c.w. operation ($\approx$ 100 days), high wall-plug efficiency (WPE = optical power/input electrical power), good beam quality, and frequency tunability. In addition, there are two system-level constraints on the frequency tuning. First, no mechanical movements should be involved for tuning the lasing frequency. Mechanical movements are often a major source of failures and not practical for unattended space/suborbital missions. Second, due to an unavoidable long optical distance between the LO and the cryocooler optical
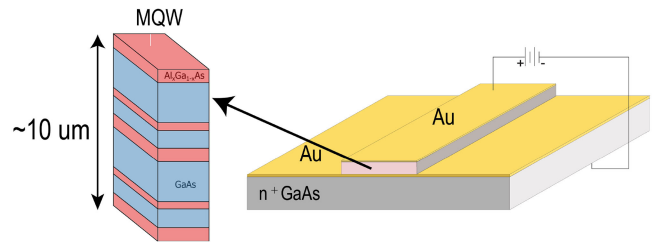

Fig. 1. Schematic of a QCL with M-M waveguide.

window, the required $\approx$ 9 GHz of frequency tuning should be ideally achieved with a single laser to minimize alignment losses. However, if multiple lasers are used (in which laser biases are electrically switched), the output power requirement linearly scales with the number of lasers to compensate the corresponding optical losses due to geometry shift. Fig. 1 shows the schematic of a QCL Fabry–Pérot (FP) device based on a metal–metal (M-M) waveguide. In this scheme, quantum wells and barriers are sandwiched between layers of metals. In THz QCLs, M-M cavities have been used to achieve higher mode confinement and lower waveguide loss [16]–[18]. These two requirements are necessary to reduce the threshold gain (G_{th}) and to achieve the maximum operating temperature (T_{max}).

In a typical THz QCL, the required molecular beam epitaxy (MBE) growth and the corresponding waveguide loss limit the active medium thickness to $\approx 10\,\mu$m $<< \lambda \approx 100\,\mu$m [19]. In addition, for proper alignment of the lasing levels in a THz QCL with a phonon depopulation scheme, which has yielded a record high $T_{max} = 250$ K [20], the voltage drop per module should be greater than the sum of longitudinal optical phonon energy in GaAs ($E_{LO} \approx 36$ meV) and emitted photon energy ≈ 14 meV. Therefore, the biasing voltage per module is ≥ 50 mV. As a result, in a typical THz QCL with $\approx$ 200 modules, the biasing voltage is typically ≥ 10 V across the device. On the other hand, the maximum current density (J_{max}) of a THz QCL is ≈ 1000 A/cm^2 that is dictated by the required high optical power and the lifetimes of lasing levels. Therefore, a millimeter-long FP device with a width of 30 μm can dissipate as much power as ≈ 5 W.

In a QCL active medium, heat is mostly carried away by acoustic phonons [21]. The heat transfer is often lower than in bulk materials as is mainly limited in the growth direction and is reduced by phonon scattering at the interface. The resultant increase in the active region temperature due to heating is detrimental to the laser performance as optical gain drops at higher temperatures. In addition to these fundamental limitations, cooling power available in the GUSTO is limited as mentioned earlier for balloon-borne missions. Therefore, choosing the best platform to achieve minimum heat dissipation while achieving higher output power in c.w. operation is crucial for the success of the GUSTO. To reduce the heat dissipation in THz QCLs, narrow waveguides (width $<< \lambda$) are often implemented. Narrow waveguides have the additional benefit of mode selectivity against undesired higher order lateral modes. The disadvantages are lower mode confinement (and consequently lower temperature performance) and poorer beam

quality. Narrow FP devices have a divergent beam pattern with a rapidly changing phase front due to subwavelength transverse dimension and interference from the front and back facets [22]. Small transverse dimensions compared to the wavelength place the THz QCL lasers in a broader class often called photonic wire lasers [23]–[27]. Photonic wire lasers are characterized as $X_\perp << \lambda$ (where $X_\perp$ is the dimension of the cross section and λ is the wavelength). In such lasers, individual sources in the laser medium emit coherently with their phases determined by the cavity modes. Consequently, each laser mode can be thought of as a continuous phased array [28].

To achieve higher mode selectivity, improved radiation efficiency, and enhanced beam quality in THz QCLs with M-M waveguides, distributed feedback (DFB) gratings with various values of $\frac{w}{\lambda} << 1$ (w is the width of waveguide) are commonly used. First-order edge-emitting DFB lasers can produce single-mode emission in c.w. operation with narrow ridges ($w < 30\,\mu$m). However, the problem of divergent radiation pattern remains for M-M waveguide devices and the outcoupling of the optical power is still low (as its efficiency) [29]. Second-order DFB cavities enable surface coupling of single-mode radiation. As the polarization of the emitted light is transverse to the light generated from the intersubband transition in a THz QCL active medium, these cavities are inherently inefficient as they possess low modal overlap. In addition, surface emission from an M-M waveguide is difficult as the light must be emitted from a metallic surface patterned with only subwavelength structures [30].

In contrast to more optimized surface emitting DFB lasers [31]–[35], edge-emitting structures are inherently have better radiation efficiency in c.w. operation. This is mainly due to the fact that the radiation originates from the same polarization generated by intersubband transition within the active medium. Therefore, edge-emitting structures with narrow cavity widths are potentially more suited for the GUSTO due to the lower electrical power dissipation, which, in turn, enables stable c.w. operation. In-plane emitting wire lasers using third-order DFB gratings [36]–[39], and along with integrated microstrip antennas [40], are the most exploited solutions since their dimensions can be scaled down without compromising the beam quality. Antenna-coupled third-order DFB (ADFB) [40] is overcoming the limitations in controlling the beam quality and radiation efficiency as compared to earlier designs [36] and has achieved as high as 0.57% wall plug efficiency in c.w. operation [40], [41]. One drawback of using ADFBs for the GUSTO is the bidirectional beam pattern. In the GUSTO, the optical power can only be collected in one direction. To improve this issue, unidirectional emission from an ADFB is highly desirable as such an emission pattern will yield a nearly factor-of-2 increase in the output power with the same heat dissipation. Lower heat dissipation enables lower base temperature and can improve the c.w. performance further. Another benefit of UADFB is the improved dynamic range required for frequency tuning using Stark shift in the active medium [21]. At the same level of output power in the forward direction, the radiation loss of a bidirectional ADFB is higher than a UADFB [8]. This often results in a lower dynamic range (higher threshold current density J_{th} and lower maximum current density J_{max}) and, consequently, a
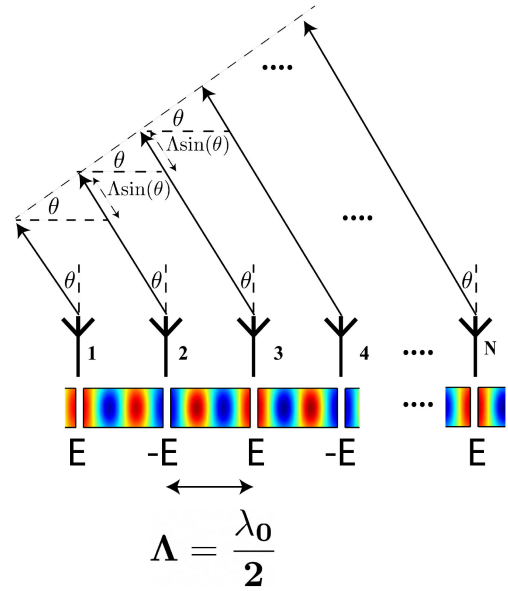

Fig. 2. Phased array antenna model for a perfectly phase matched third-order DFB with N elements.

lower frequency tuning range in an ADFB as compared to that of a UADFB. In [8], the power of the forward-emitting laser was increased by a factor of 1.8 compared to a reference bidirectional DFB laser. The UADFB platform has achieved the record high c.w. power wall plug efficiency of $\approx 1\%$, which is crucial for GUSTO.

C. UADFB for the GUSTO

A perfectly phase matched third-order DFB laser can be modeled as an array of evenly distributed radiators with a π phase difference between adjacent radiators [37], [38]. A simple 1-D model for this phased array antenna is shown in Fig. 2. It is well known that the radiation field of a linear antenna array is the product of the array factor (AF) and the element factor (EF). The AF is a function of the positions of the antennas in the array and the weights. The EF is the radiation pattern of individual elements in the presence of all other elements (in the case of interacting elements). It can be shown [42] that the AF for a uniform amplitude 1-D antenna array is

$$|\text{AF}|^2 = \left| \frac{1}{N} \frac{\sin\left(\frac{N\Psi}{2}\right)}{\sin\left(\frac{\Psi}{2}\right)} \right|^2. \tag{1}$$

Here, N is the number of elements (periods) and Ψ is defined as

$$\Psi = 2\pi \frac{\Lambda}{\lambda_0} \sin(\theta) + \pi. \tag{2}$$

In a perfectly phase matched third-order DFB laser, the periodicity (Λ) is $\frac{\lambda_0}{2}$, where λ_0 is the free-space radiation wavelength
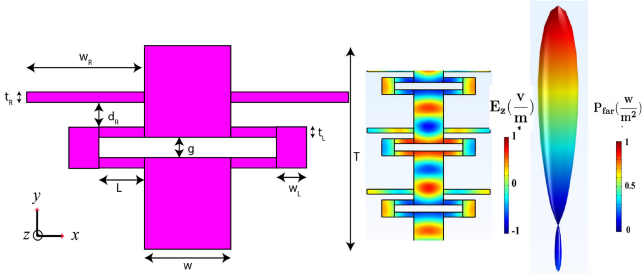
Fig. 3. Simulation for mode profile and far-field beam pattern for an optimized UADFB at 4.75 THz. The mask parameters are $w_R = 20.5$, $t_R = 2.5$, $d_R = 3$, $t_L = 2.5$, $g = 3.75$, $L = 8.5$, $w_L = 5.5$, $w = 13$, and $T = 31.5$. All units are in micrometers. The number of periods is $N = 30$, but only three periods are shown to fit in the figure. $n_{GaAs} = 3.66$ were used for simulations.

of the laser. This simplifies (2) as

$$\Psi = \pi \sin(\theta) + \pi. \tag{3}$$

A tighter beam can be achieved with more elements within the array provided that the phase matching condition is met. For a third-order DFB, a figure of merit for the phase matching condition is defined as

$$n_{\text{eff}} = 3 \frac{\lambda_0}{2\Lambda}. \tag{4}$$

In a perfectly phase matched third-order DFB, the effective modal index $n_{\text{eff}} = 3$. Deviation from this optimal value results in accumulated phase mismatch between the free-space wave and the wave traveling inside the semiconductor and degrades the beam quality for longer arrays, which are often required for tighter beam patterns.

Compared to a third-order DFB shown in Fig. 2, in a UADFB, an asymmetric EF is used to "skew" the bidirectional EF into unidirectional [8]. The asymmetric EF is implemented using reflectors defined with (w_R, t_R, d_R) in Fig. 3. The antenna loop around the radiation gaps, defined with (L, w_L, t_L), is used to increase the radiation surface and improve efficiency [38]. A 3-D simulation of a UADFB structure can be performed using quasi-eigenmode solvers of commercially available electromagnetic simulators. Fig. 3 shows the computed mode distribution and the corresponding unidirectional radiation pattern for an UADFB at 4.75 THz using the COMSOL package.

D. Frequency Adjustment of UADFBs

Fabrication fluctuation (change in the dimensions due to photo lithography and etching, sidewall slopes, and roughness) and the change in the center gain of an active medium in different MBE growth can produce as large as ≈ 200 GHz change in the lasing frequency of a fabricated UADFB as compared to simulations and prior fabrications of the same design. Though full-wave 3-D simulations can provide a good starting point for experimental demonstrations, they are often inadequate to predict gigahertz-level (10^9 Hz) accuracy. Therefore, coarse (≈ 100 GHz) and fine adjustment (≈ 4 GHz) of lasing frequency is required to achieve the accuracy of ≈ 4 GHz required in the GUSTO. The UADFB cavity width (w), the length of antenna loop (L), the

periodicity (T), and the size of the gap between microcavities (g) are the major adjusting parameters of the lasing frequency in a UADFB [41] and are shown in Fig. 3. Adjusting the lasing frequency through each of these variables comes with certain advantages and limitations.

The width of microcavities can be used to tune the lasing frequency ($w\downarrow f\uparrow$, $w\uparrow f\downarrow$). This approach is similar to adjusting the cutoff frequency of rectangular waveguides in microwave waveguides [43]. Wider cavities ($w\uparrow$) are prone to undesired higher order lateral mode overlap with the fundamental mode, while narrower cavities ($w\downarrow$) are prone to a lower mode confinement factor [44] and susceptible to higher loss due to roughness of sidewalls. By proper design, the cavity width can be used to achieve discrete frequency change in the order of ≈ 100 GHz.

The length of the antenna loop (L) can be used to tune the lasing frequency ($L\downarrow f\uparrow$, $L\uparrow f\downarrow$). However, as the antenna length defines the radiation surface in an ADFB [38], variation in the device performance will be significant. More specifically, for UADFB design, there is an optimal L for achieving the highest asymmetry ratio in the forward direction [8]. Therefore, L is not used here for frequency tuning in an UADFB.

Antenna gap size can also be used to tune the lasing frequency ($g\uparrow f\uparrow$, $g\downarrow f\downarrow$). However, large frequency tuning leads to significant change in the output power. Therefore, variation in g is not used for frequency adjustment. It is worth mentioning that g is the main parameter, which controls the radiation loss and, therefore, the output power and maximum lasing temperature. This parameter should be optimized to achieve the required temperature and power performance.

Fine adjusting the periodicity (T) is a reliable strategy to fine adjust the lasing frequency ($T\downarrow f\uparrow$, $T\uparrow f\downarrow$). Since deviating from $n_{\text{eff}} = 3$ reduces the beam quality, an accurate simulation to minimize the index mismatch is necessary for an optimal design.

E. Design Strategy

The major design strategy is to fabricate multiple DFB arrays with a defined geometry relation between elements on the same sample (≈ 1.3 cm $\times$ 1.3 cm). The width of microcavities is used to achieve large discrete frequency change at the center of each DFB array (≈ 100 GHz with $\approx 1\mu m$ change in w) and the periodicity is used (30-nm steps) within each array to achieve ≈ 4 GHz change in the lasing frequency. Within the same sample, the gap size (g) should also be adjusted to achieve the required c.w. performance listed in Table I. A wider gap results in a greater radiation loss and will yield a higher power level at lower temperatures, but it will also reduce the power at higher temperatures due to limited gain at 50 K. A photolithography mask used for the GUSTO is shown in Fig. 4. Each DFB array consists of 18 DFBs, which are closely spaced ($\approx 250\,\mu m$ apart), and their lasing frequency is finely adjusted by ≈ 4 GHz through the change in their periodicity. The choice of 18 DFBs per array is to ensure minimum wire bonding angles and uniformity in the indium bonding during the subsequent mounting process. An example of such array is shown in Fig. 4. To achieve ≈ 4 GHz frequency tuning in a UADFB at 4.7 THz, the change in the periodicity is ≈ 30 nm, which is much finer than the absolute
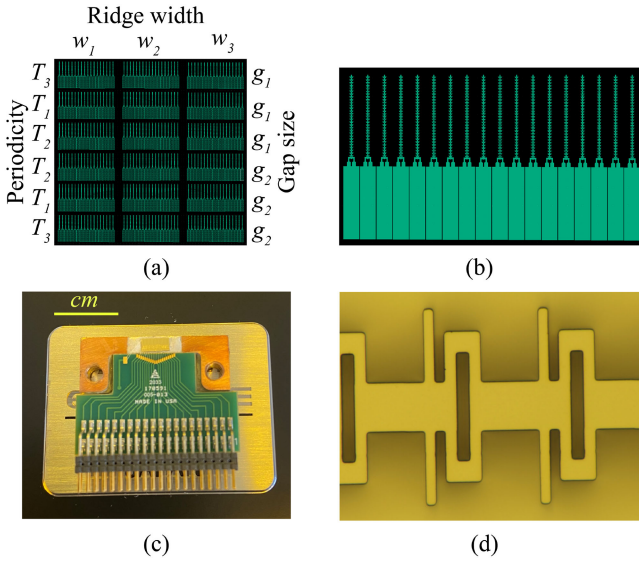
Fig. 4.   (a) Fabrication mask to cover $\approx$ 300 GHz. w_1 = 12.5, w_2 = 13, w_3 = 13.5, g_1 = 3.75, g_2 = 4, T_1 = range[30.77–0.03–31.3], T_2 = range[31.33–0.03–31.85], and T_3 = range[31.88–0.03–32.4]. All the units are in the dimension of micrometers. Parameters are defined in Fig. 3 and the number of periods is 30. The patterned area size is $\approx$ 1 cm^2, which yields a frequency coverage per unit area of $\approx$ 300 GHz/cm^2. (b) Single DFB array showing 18 UADFBs. (c) Heatsink and electronic printed circuit board for wire bonding. (d) Optical image for three periods of a fabricated UADFB.

Fig. 5.   Light–current with measured frequencies indicated in the inset. The mask parameters are w_R = 20.5, t_R = 2.5, d_R = 3, t_L = 2.5, g = 3.75, L = 8.5, w_L = 5.5, w = 13, and T = 31.5. All units are in micrometers, and the number of periods is N = 30. The maximum bias voltage is $\approx$ 13 V.

Fig. 6.   Measured voltage–current and beam pattern as inset. The beam pattern is measured through a rectangular raster scan at $\approx$ 41 mm distance from the device. For this device, n_{eff} = 3.01.

resolution achievable by photolithography. For example, the MLA150 maskless aligner used at MIT cleanroom has a nominal 1-μm resolution. Though far below the resolution, the relative change in the periodicity between neighboring devices in the photolithography mask will produce a relative change in the exposure dose. Such changes in the exposure dose will ultimately impact the device geometry and fine adjust the frequency almost monotonically. The unavoidable mistargeting will be made up with a different array. The benefit of avoiding electron beam lithography is to achieve a thicker metal stack ($\geq$ 300 nm) for c.w. reliability and to process larger samples that are required to cover a large frequency range.

III. EXPERIMENTAL RESULTS

The light–current spectrum results for a flight ready device are shown in Fig. 5. This sample is fabricated on a wafer based on a modified version of a design proposed in [45]. The original 15% barrier suggested in this article did not produce satisfactory results in the MBE chambers at Sandia National Laboratories and at the University of Waterloo. The frequencies of peak gain (4.1–4.2 THz, measured with FP devices) are too far below the target frequency of 4.7 THz. Guided by simulation, by increasing the barrier composition to 17%, the gain peak was shifted higher to $\approx$ 4.5 THz. The final flight-ready devices were fabricated on a wafer labeled VB1053 grown at Sandia National Laboratories.

Though the neighboring devices have $\approx$ 4 GHz frequency spacing, a combination of red shift in lasing frequency with temperature and blue shift with electrical bias (Stark shift) in one of the 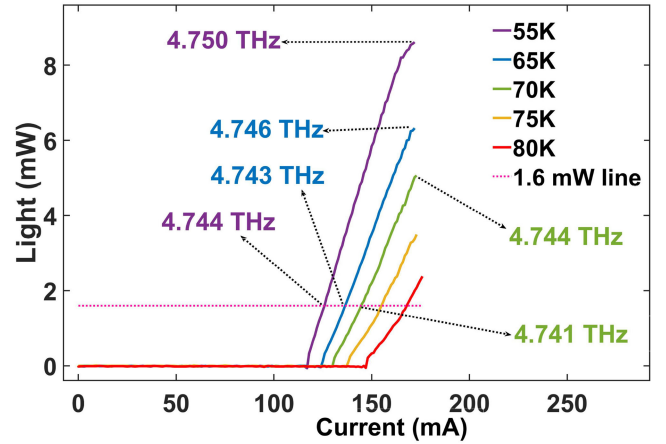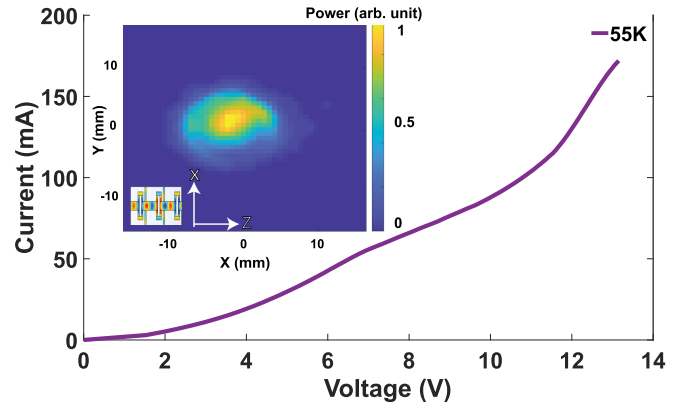UADFB devices could cover the entire frequency band required by the GUSTO. The large tuning with electrical bias is inherent in intersubband lasers [21]. However, larger tuning with injection requires high dynamic range, high power, and a robust single-mode operation offered in the UADFB platform. As n_{eff} = 3.01 for this device, a tight single-lobe beam is achieved. The measured beam pattern without any collimating optics is shown in Fig. 6.

IV. CONCLUSION

In this article, we demonstrated a tunable high-power source for the LO at 4.744 THz for the GUSTO using THz QCL with a novel UADFB design. UADFB offers high c.w. efficiency, tight beam pattern, and frequency tunability. Though THz QCL has been mainly a research subject since its invention 20 years ago, the GUSTO is a unique opportunity to demonstrate the potentials of this platform for real-world applications.

TABLE II
DEVELOPED QCLS AT 4.744 THZ FOR SOFIA AND STO-2

Reference	type	c.w. power at 50 K
SOFIA[10]	First order Grating	$\approx 150\ \mu$W
SOFIA[11]	First order Grating	$\approx 200\ \mu$W
STO-2[41]	Third order Grating	$\approx 250\ \mu$W

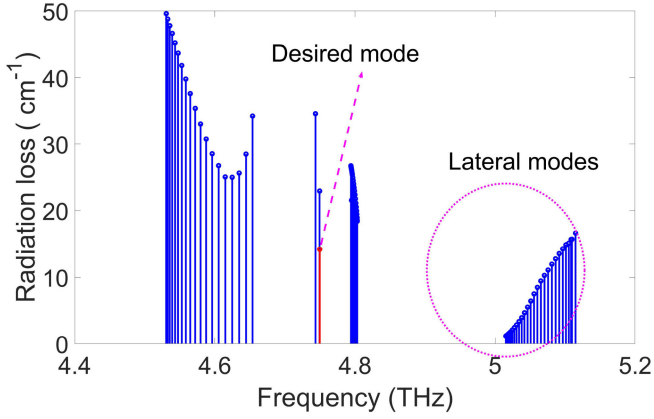Fig. 7. Eigenmode simulation. Only modes with radiation loss ≤ 50 cm^{-1} are shown. The mask parameters are $w_R = 20.5$, $t_R = 2.5$, $d_R = 3$, $t_L = 2.5$, $g = 3.75$, $L = 8.5$, $w_L = 5.5$, $w = 13$, and $T = 31.5$. All units are in micrometers.

V. SUPPLEMENTARY MATERIALS

A. Summary of Developed QCLs for SOFIA and STO-2

A summary of developed QCLs at 4.744 THz for SOFIA and STO-2 is provided in Table II.

B. Simulation

Using 3-D FEM simulation, quasi-eigenmodes of the whole antenna-coupled laser structures can be found with detailed information of both the electric and magnetic field distributions both inside the cavity and also in the far field. From the complex eigenfrequencies, we can estimate the mode frequency and the corresponding radiation losses. The simulations were carried out using COMSOL Multiphysics version 5.3. No metal losses and material losses were taken into account when performing the "cold cavity" eigenmode simulation. The simulation environment was surrounded with a perfectly matched layer to absorb nonphysical reflections from the boundaries. The boundaries were chosen to be at least $\frac{\lambda_0}{2}$ away from the laser in each dimension. The structure was meshed symmetrically using dummy reflectors with a refractive index of 1 and mesh copy capabilities to mesh the structure symmetrically. This scheme is important to avoid any digital artifacts caused by asymmetric meshing. The mesh is chosen to be smaller than $\frac{\lambda}{10}$, in which λ is the wavelength in the corresponding medium. The mirror loss was calculated from the imaginary part of the complex eigenfrequency (f_i) using $\alpha_m = 4\pi n_r \frac{f_i}{c}$, where c is the speed of light and n_r is the real part of the GaAs refractive index that was set to 3.66. The radiation loss for the flight device is shown in Fig. 7.

C. Measurement Methods

The current in Fig. 5 is measured using a calibrated 2230G-30-3 Keithley DC Power Supply. The light was measured using a room temperature pyroelectric detector (from QMC Instruments Ltd. with a noise equivalent power of ≈ 460 pW/$\sqrt{\text{Hz}}$) and calibrated using a power meter developed by Thomas Keating Ltd. Spectra were measured using a Fourier transform infrared spectrometer (model Thermo Nicolet 8700) with an internal deuterated triglycine sulfate detector. Far-field beam patterns were measured with a pyroelectric detector mounted on a 2-D motorized scanning stage that was placed at 41 mm from the lasers scanning between ± 25 mm for both directions without any optics between the laser and the detector. The laser was operated near the peak power in pulsed mode with 10% duty cycle and electronically chopped at 100 Hz.

D. Fabrication

From the MBE wafers, samples of typical size 1.5 $\times$1.5 cm^2 were cleaved. In addition to the cleaved MBE samples, a slightly larger $n+$ GaAs substrate (from AXT, Inc.) was used as a receptor substrate onto which the MBE-grown wafer was bonded. Ta (12 nm)/Au (280 nm) was evaporated onto both the MBE sample and the receptor substrate in an $\approx 5 \times 10^{-7}$ torr vacuum at a rate of 1 A$^\circ$/s. The MBE sample and the receptor were then bonded together using an M-M thermocompression at 300 $^\circ$C and 4 MPa of pressure for 1 h in vacuum. Then, the samples were annealed at the same temperature, but in atmospheric pressure nitrogen (N_2) and with no applied force for 45 min. Compressible graphite spacers were used to distribute the force uniformly during bonding. Following wafer bonding, the native MBE substrate was lapped down to a thickness of $\approx 100\ \mu$m. The remaining MBE substrate was then removed by wet etching in a 4:1 (by volume) solution of citric acid (1 g/mL) and 20% hydrogen peroxide (H_2O_2), which stops selectively at the $Al_{0.55}Ga_{0.45}As$ etch-stop layer. The exposed etch-stop layer was then selectively removed by concentrated (49%) hydrofluoric acid. 250 nm of low-stress silicon nitride was then deposited at 300 $^\circ$C for bonding pad definitions using STS-CVD . SPR700 photoresist was used to define the bonding pad and excess nitride was etched away in Ar/CF$_4$ plasma. The top $n+$ contact was partially removed by a solution of $H_3PO_4(1)/H_2O_2(1)/H_2O(25)$ to minimize the damage to $n+$ layer due to fluorine ion diffusion. The top contact/waveguide metal was then defined by a bilayer liftoff process (double coating of PMGI-SF5 and SPR700). The final top metallization layer was Ta (12 nm)/Au(300 nm), deposited under the same conditions as the first evaporation. Extra evaporation steps were performed to increase the metal thickness on bonding pads to 1 μm using AZ5214 negative photoresist. Increasing the bonding pad metal thickness is crucial to avoid bonding pad failure in c.w. operation, since two wire bonds per pad are required for the GUSTO. Excess silicon nitride was etched in Ar/CF$_4$ plasma for which the top Au acts as a self-aligned mask. Samples were cleaned with extended oxygen plasma to remove passivations formed during Ar/CF$_4$ etching. The waveguide was then defined through dry etching in Cl$_2$:SiCl$_4$:Ar plasma, for which the top Au acts as a self-aligned mask. To avoid chamber

contamination due to gold particles, the chamber was cleaned at 300 °C using Ar/Cl_2 plasma. The dry etch recipe achieved vertical sidewalls due to the formation of a protective Si-based film during the etch. The sidewall passivation was removed by immersion in buffered-oxide etchant. The receptor wafer was then lapped down to $\approx 190~\mu$m, and its backside is metalized with Ti(10 nm)/Au(150 nm) at $\approx 1 \times 10^{-6}$ torr vacuum with a 2 A°/s deposition rate. The improved quality of wafer bonding using graphite spacers and optimized lithography process has produced fabrication yield $\geq 95\%$.

ACKNOWLEDGMENT

REFERENCES

[1] A. G. Tielens, *The Physics and Chemistry of the Interstellar Medium*. Cambridge, U.K.: Cambridge Univ. Press., 2005.

[2] G. Dodel, "On the history of far-infrared (FIR) gas lasers: Thirty-five years of research and application," *Infrared Phys. Technol.*, vol. 40, no. 3, pp. 127–139, 1999.

[3] R. Köhler *et al.*, "Terahertz semiconductor-heterostructure laser," *Nature*, vol. 417, no. 6885, pp. 156–159, 2002.

[4] L. Rezac *et al.*, "First detection of the 63 μ m atomic oxygen line in the thermosphere of mars with GREAT/SOFIA," *Astron. Astrophys.*, vol. 580, 2015, Art. no. L10.

[5] C. Walker *et al.*, "The stratospheric THz observatory (STO)," in *Ground-Based and Airborne Telescopes III*, vol. 7733. Bellingham, WA, USA: International Society for Optics and Photonics, 2010, Art. no. 77330N.

[6] C. K. Walker *et al.*, "GUSTO: Gal/Xgal U/LDB spectroscopic-stratospheric terahertz observatory," in *Proc. Amer. Astronom. Soc. Meeting Abstr.*, 2018, vol. 231, pp. 231–05.

[7] P. N. Bernasconi, C. K. Walker, C. Kulesa, and P. Goldsmith, "The GUSTO balloon mission," in *Proc. AGU Fall Meeting Abstr.*, 2019, vol. 2019, pp. A 33Q–2940.

[8] A. Khalatpour, J. L. Reno, N. P. Kherani, and Q. Hu, "Unidirectional photonic wire laser," *Nature Photon.*, vol. 11, no. 9, pp. 555–559, 2017.

[9] C. Risacher *et al.*, "The upGREAT dual frequency heterodyne arrays for SOFIA," *J. Astronom. Instrum.*, vol. 7, no. 4, 2018, Art. no. 1840014.

[10] H. Richter *et al.*, "4.7 THz local oscillator for the GREAT heterodyne spectrometer on SOFIA," *IEEE Trans. THz Sci. Technol.*, vol. 5, no. 4, pp. 539–545, Jul. 2015.

[11] L. Bosco *et al.*, "A patch-array antenna single-mode low electrical dissipation continuous wave terahertz quantum cascade laser," *Appl. Phys. Lett.*, vol. 109, no. 20, 2016, Art. no. 201103.

[12] J. W. Goodman, *Introduction to Fourier Optics*. Greenwood Village, CO, USA: Roberts and Company Publishers, 2005.

[13] B. Mirzaei *et al.*, "8-beam local oscillator array at 4.7 THz generated by a phase grating and a quantum cascade laser," *Opt. Exp.*, vol. 25, no. 24, pp. 29 587–29596, 2017.

[14] J. Silva *et al.*, "Preliminary design study of a 4 HEB array at 4.7 THz for GUSTO," in *Proc. 29th Int. Symp. Space THz Technol.*, Pasadena, CA, USA, 2018, pp. 82–86.

[15] Y. Gan *et al.*, "81 supra-THz beams generated by a fourier grating and a quantum cascade laser," *Opt. Exp.*, vol. 27, no. 23, pp. 34 192–34203, 2019.

[16] K. Unterrainer *et al.*, "Quantum cascade lasers with double metal-semiconductor waveguide resonators," *Appl. Phys. Lett.*, vol. 80, no. 17, pp. 3060–3062, 2002.

[17] B. S. Williams, S. Kumar, H. Callebaut, Q. Hu, and J. L. Reno, "Terahertz quantum-cascade laser at $\lambda \approx 100~\mu$m using metal waveguide for mode confinement," *Appl. Phys. Lett.*, vol. 83, no. 11, pp. 2124–2126, 2003.

[18] B. S. Williams, S. Kumar, Q. Hu, and J. L. Reno, "Operation of terahertz quantum-cascade lasers at 164 K in pulsed mode and at 117 K in continuous-wave mode," *Opt. Exp.*, vol. 13, no. 9, pp. 3331–3339, 2005.

[19] Z. Wasilewski, "MBE growth of THz quantum cascade lasers," in *Molecular Beam Epitaxy*. Amsterdam, The Netherlands: Elsevier, 2013, pp. 631–655.

[20] A. Khalatpour, A. K. Paulsen, C. Deimert, Z. R. Wasilewski, and Q. Hu, "High-power portable terahertz laser systems," *Nature Photon.*, vol. 15, no. 1, pp. 16–20, 2021.

[21] J. Faist, *Quantum Cascade Lasers*. Oxford, U.K.: Oxford Univ. Press, 2013.

[22] A. Adam *et al.*, "Beam patterns of terahertz quantum cascade lasers with subwavelength cavity dimensions," *Appl. Phys. Lett.*, vol. 88, no. 15, 2006, Art. no. 151105.

[23] M. T. Hill and M. C. Gather, "Advances in small lasers," *Nature Photon.*, vol. 8, no. 12, pp. 908–918, 2014.

[24] M. Noginov *et al.*, "Demonstration of a spaser-based nanolaser," *Nature*, vol. 460, no. 7259, pp. 1110–1112, 2009.

[25] R. F. Oulton *et al.*, "Plasmon lasers at deep subwavelength scale," *Nature*, vol. 461, no. 7264, pp. 629–632, 2009.

[26] J. Zhang *et al.*, "Photonic-wire laser," *Phys. Rev. Lett.*, vol. 75, no. 14, 1995, Art. no. 2678.

[27] M. T. Hill *et al.*, "Lasing in metallic-coated nanocavities," *Nature Photon.*, vol. 1, no. 10, pp. 589–594, 2007.

[28] E. Orlova *et al.*, "Antenna model for wire lasers," *Phys. Rev. Lett.*, vol. 96, no. 17, 2006, Art. no. 173904.

[29] B. S. Williams, S. Kumar, Q. Hu, and J. L. Reno, "Distributed-feedback terahertz quantum-cascade lasers with laterally corrugated metal waveguides," *Opt. Lett.*, vol. 30, no. 21, pp. 2909–2911, 2005.

[30] S. Kumar *et al.*, "Surface-emitting distributed feedback terahertz quantum-cascade lasers in metal-metal waveguides," *Opt. Exp.*, vol. 15, no. 1, pp. 113–128, 2007.

[31] S. Biasco *et al.*, "Highly efficient surface-emitting semiconductor lasers exploiting quasi-crystalline distributed feedback photonic patterns," *Light: Sci. Appl.*, vol. 9, no. 1, pp. 1–11, 2020.

[32] S. Biasco *et al.*, "Continuous-wave highly-efficient low-divergence terahertz wire lasers," *Nature Commun.*, vol. 9, no. 1, pp. 1–8, 2018.

[33] Y. Jin *et al.*, "High power surface emitting terahertz laser with hybrid second-and fourth-order Bragg gratings," *Nature Commun.*, vol. 9, no. 1, 2018, Art. no. 1407.

[34] C. A. Curwen, J. L. Reno, and B. S. Williams, "Terahertz quantum cascade VECSEL with watt-level output power," *Appl. Phys. Lett.*, vol. 113, no. 1, 2018, Art. no. 011104.

[35] G. Xu *et al.*, "Surface-emitting terahertz quantum cascade lasers with continuous-wave power in the tens of milliwatt range," *Appl. Phys. Lett.*, vol. 104, no. 9, 2014, Art. no. 091112.

[36] M. I. Amanti, M. Fischer, G. Scalari, M. Beck, and J. Faist, "Low-divergence single-mode terahertz quantum cascade laser," *Nature Photon.*, vol. 3, no. 10, pp. 586–590, 2009.

[37] M. I. Amanti, G. Scalari, F. Castellano, M. Beck, and J. Faist, "Low divergence terahertz photonic-wire laser," *Opt. Exp.*, vol. 18, no. 6, pp. 6390–6395, 2010.

[38] T.-Y. Kao, Q. Hu, and J. L. Reno, "Perfectly phase-matched third-order distributed feedback terahertz quantum-cascade lasers," *Opt. Lett.*, vol. 37, no. 11, pp. 2070–2072, 2012.

[39] M. Wienold *et al.*, "High-temperature, continuous-wave operation of terahertz quantum-cascade lasers with metal-metal waveguides and third-order distributed feedback," *Opt. Exp.*, vol. 22, no. 3, pp. 3334–3348, 2014.

[40] T.-Y. Kao, X. Cai, A. W. Lee, J. L. Reno, and Q. Hu, "Antenna coupled photonic wire lasers," *Opt. Exp.*, vol. 23, no. 13, pp. 17 091–17100, 2015.

[41] T.-Y. Kao, "From high power terahertz quantum cascade lasers to terahertz light amplifiers," Ph.D. dissertation, Massachusetts Inst. Technol., 2014.

[42] C. A. Balanis, *Antenna Theory: Analysis and Design*. Hoboken, NJ, USA: Wiley, 2016.

[43] R. F. Harrington, *Time-Harmonic Electromagnetic Fields*. New York, NY, USA: McGraw-Hill, 1961.

[44] N. Han *et al.*, "Broadband all-electronically tunable MEMS terahertz quantum cascade lasers," *Opt. Lett.*, vol. 39, no. 12, pp. 3480–3483, 2014.

[45] K. Ohtani *et al.*, "High performance 4.7 THz GaAs quantum cascade lasers based on four quantum wells," *New J. Phys.*, vol. 18, no. 12, 2016, Art. no. 123004.